

Article

Enhancing Soil Salinity Evaluation Accuracy in Arid Regions: An Integrated Spatiotemporal Data Fusion and AI Model Approach for Arable Lands

Tong Su ¹, Xinjun Wang ^{1,*}, Songrui Ning ² , Jiandong Sheng ¹, Pingan Jiang ¹, Shenghan Gao ¹, Qiulan Yang ¹, Zhixin Zhou ¹, Hanyu Cui ¹ and Zhilin Li ¹

¹ Xinjiang Key Laboratory of Soil and Plant Ecological Processes, Xinjiang Engineering Technology Research Center of Soil Big Data, Xinjiang Agricultural University, Urumqi 830052, China; st3960039600@gmail.com (T.S.); sjd@xjau.edu.cn (J.S.); jpa@xjau.edu.cn (P.J.); gaozj6542@gmail.com (S.G.); yql18884@163.com (Q.Y.); 19862113650@163.com (Z.Z.); cuihanyu1999@163.com (H.C.); 15511488270@163.com (Z.L.)

² State Key Laboratory of Eco-Hydraulics in Northwest Arid Region of China, Xi'an University of Technology, Xi'an 710048, China; ningsongrui@163.com

* Correspondence: wangxj@xjau.edu.cn

Abstract: Soil salinization is one of the primary factors contributing to land degradation in arid areas, severely restricting the sustainable development of agriculture and the economy. Satellite remote sensing is essential for real-time, large-scale soil salinity content (SSC) evaluation. However, some satellite images have low temporal resolution and are affected by weather conditions, leading to the absence of satellite images synchronized with ground observations. Additionally, some high-temporal-resolution satellite images have overly coarse spatial resolution compared to ground features. Therefore, the limitations of these spatiotemporal features may affect the accuracy of SSC evaluation. This study focuses on the arable land in the Manas River Basin, located in the arid areas of northwest China, to explore the potential of integrated spatiotemporal data fusion and deep learning algorithms for evaluating SSC. We used the flexible spatiotemporal data fusion (FSDAF) model to merge Landsat and MODIS images, obtaining satellite fused images synchronized with ground sampling times. Using support vector regression (SVR), random forest (RF), and convolutional neural network (CNN) models, we evaluated the differences in SSC evaluation results between synchronized and unsynchronized satellite images with ground sampling times. The results showed that the FSDAF model's fused image was highly similar to the original image in spectral reflectance, with a coefficient of determination (R^2) exceeding 0.8 and a root mean square error (RMSE) below 0.029. This model effectively compensates for the missing fine-resolution satellite images synchronized with ground sampling times. The optimal salinity indices for evaluating the SSC of arable land in arid areas are S3, S5, SI, SI1, SI3, SI4, and Int1. These indices show a high correlation with SSC based on both synchronized and unsynchronized satellite images with ground sampling times. SSC evaluation models based on synchronized satellite images with ground sampling times were more accurate than those based on unsynchronized images. This indicates that synchronizing satellite images with ground sampling times significantly impacts SSC evaluation accuracy. Among the three models, the CNN model demonstrates the highest predictive accuracy in SSC evaluation based on synchronized and unsynchronized satellite images with ground sampling times, indicating its significant potential in image prediction. The optimal evaluation scheme is the CNN model based on satellite image synchronized with ground sampling times, with an R^2 of 0.767 and an RMSE of $1.677 \text{ g} \cdot \text{kg}^{-1}$. Therefore, we proposed a framework for integrated spatiotemporal data fusion and CNN algorithms for evaluating soil salinity, which improves the accuracy of soil salinity evaluation. The results provide a valuable reference for the real-time, rapid, and accurate evaluation of soil salinity of arable land in arid areas.

Keywords: soil salinization; manas river basin; satellite images evaluation; deep learning; arid region



Citation: Su, T.; Wang, X.; Ning, S.; Sheng, J.; Jiang, P.; Gao, S.; Yang, Q.; Zhou, Z.; Cui, H.; Li, Z. Enhancing Soil Salinity Evaluation Accuracy in Arid Regions: An Integrated Spatiotemporal Data Fusion and AI Model Approach for Arable Lands. *Land* **2024**, *13*, 1837. <https://doi.org/10.3390/land13111837>

Academic Editors: Tiago Brito Ramos, Maria da Conceição Gonçalves and Mohammad Farzamian

Received: 18 September 2024

Revised: 29 October 2024

Accepted: 30 October 2024

Published: 5 November 2024



Copyright: © 2024 by the authors. Licensee MDPI, Basel, Switzerland. This article is an open access article distributed under the terms and conditions of the Creative Commons Attribution (CC BY) license (<https://creativecommons.org/licenses/by/4.0/>).

1. Introduction

Soil salinization is a significant global ecological issue and a major cause of soil degradation [1]. It often leads to reduced water resource utilization, decreased soil quality, and stunted crop growth [2]. The impact of soil salinization is particularly acute in the arable land of arid areas. In addition to factors such as climate, soil type, and groundwater, improper irrigation practices accelerate soil salinization, severely hindering sustainable agricultural development in irrigated areas [3,4]. Therefore, the accurate evaluation of soil salinization information is fundamental for guiding farmland management and salinization prevention. Compared to traditional soil sampling methods, using satellite images for evaluation is currently the primary method for rapid, large-scale soil salinization monitoring.

Many scholars have conducted extensive research on using satellite images to evaluate soil salinization [5,6]. Based on the sensor source of the satellite images, the soil salinity content (SSC) evaluation methods are mainly divided into two categories. The first category is the SSC evaluation method based on single-source satellite images [7]. This method uses satellite images from a single sensor to establish a model for evaluating SSC by leveraging the relationship between the image's reflectance spectrum and surface SSC [8,9]. For instance, Whitney et al. [10] used MODIS images to develop an SSC evaluation model for the semi-arid region of California, USA, enabling rapid and wide-scale SSC evaluation. Sahbeni et al. [11] effectively evaluated SSC in the Hungarian plain using Landsat-8 OLI images. Although modeling based on single-source satellite images is efficient and straightforward, some satellite images (such as Landsat-8 OLI) have low temporal resolution (16 days) and are affected by weather conditions, leading to the absence of satellite images synchronized with ground observations. Additionally, some high-temporal-resolution satellite images (such as MODIS) have overly coarse spatial resolution compared to ground features [12]. The limitations of these spatiotemporal features may affect the accuracy of the satellite image evaluation of SSC. To overcome these limitations, scholars have proposed a second method: SSC evaluation based on multi-source satellite image fusion [13]. This method uses mathematical algorithms to fuse spatiotemporal information from different sensor satellite images, producing fine-resolution images synchronized with the ground SSC acquisition times, thereby enabling SSC evaluation [14]. For instance, Zhao et al. [15] used various spatiotemporal fusion methods to fuse MODIS and Landsat-8 OLI images, generating satellite images synchronized with ground sampling times. The results demonstrated a significant improvement in SSC evaluation accuracy based on fused images. However, the effectiveness of spatiotemporal fusion methods is closely related to surface conditions [16]. Currently, research on multi-source satellite spatiotemporal fusion methods for soil salinity evaluation is mainly focused on the peak growing season of crops when the surface typically has high vegetation cover, and spectral information primarily comes from the crops [17]. However, during the early stages of crop growth with low vegetation cover, spectral information includes both crops and bare soil, and research on spatiotemporal fusion methods at this stage remains limited. Therefore, the application of multi-source satellite image fusion in the evaluation of soil salinity in arable land in arid areas requires further exploration.

The accuracy of evaluating SSC using satellite images is influenced not only by the spatiotemporal features of the images but also by spectral features and seasonal vegetation cover changes [18,19]. Different spectral indices sensitive to SSC vary under different surface conditions. This is because surface features and vegetation cover alter the reflection and absorption characteristics of the spectra, thereby affecting the sensitivity of spectral indices to SSC [20]. For instance, Khan et al. [21] proposed the normalized difference salinity index (NDSI) and the salinity index (SI), which can effectively evaluate SSC in bare soils with low vegetation cover. Bouaziz et al. [22] found that in areas with higher vegetation cover, salinity indices (SI 1, SI 2, SI 3) showed strong correlations with SSC, making them suitable for SSC evaluation during the crop growth season. Although various salinity indices have been proposed and have shown high accuracy in evaluating SSC in different regions, uncertainty remains regarding which indices are most suitable for evaluating SSC

in arable land in arid areas. Therefore, further validation and research are needed. Besides the temporal and spectral features of satellite images, the chosen algorithm significantly impacts the accuracy of SSC evaluation results [23,24]. Different algorithms vary in their data processing strategies and efficiencies, making the selection of an appropriate algorithm crucial for improving evaluation accuracy [25]. Machine learning algorithms are widely applied in this field due to their adaptability and modeling flexibility. These methods can handle multidimensional input features and provide relatively accurate predictions [26,27]. For instance, Chen et al. [28] constructed SSC evaluation models using multiple linear regression (MLR), back propagation neural networks (BPNNs), and SVR algorithms in the coastal area of the Yellow River Delta. They found that the SVR model had the highest accuracy, with an R^2 of 0.78 and an RMSE of $3.02 \text{ g}\cdot\text{kg}^{-1}$. Fathizad et al. [29] effectively evaluated soil salinity in the central desert of Iran using the RF model. Although traditional machine learning algorithms perform exceptionally well in certain cases, particularly when datasets are small or feature dimensions are relatively simple, they often face limitations when dealing with complex spatial structures and changes. These limitations include low computational efficiency and difficulty in capturing nonlinear relationships and spatial feature changes [30,31]. In contrast, deep learning algorithms have shown significant advantages in handling complex, large-scale satellite data. Wang et al. [32] discovered that CNN models exhibited strong predictive performance for soil salinity in the desert oasis region of northwest China. This is because the deep structure of CNN models can automatically extract complex spatial features from satellite images, enhancing the model's robustness. This capability is particularly effective when dealing with heterogeneous regions of soil and vegetation coverage, making CNN an ideal tool for SSC evaluation under complex surface conditions [33]. However, the spectral features of satellite images with different temporal features may affect the accuracy of evaluation results. Therefore, proposing a scheme of integrated spatiotemporal data fusion and deep learning algorithms to enhance the accuracy of soil salinity evaluation of arable land in arid areas remains a subject requiring extensive research and exploration.

Therefore, to improve the accuracy of arable land soil salinity evaluation, this study explores the applicability of integrating spatiotemporal data fusion and deep learning algorithms for evaluating soil salinity in arid areas. In this study, the soil salinity content (SSC) at a depth of 0–30 cm in cotton fields was taken as the research object. The optimal salinity indices were selected based on satellite images synchronized and unsynchronized with ground sampling times, and a variety of soil salinity evaluation models were constructed. The purposes of this study were to (1) evaluate the impact of synchronicity between satellite imagery spectral features and ground sampling times on the accuracy of SSC evaluation; (2) validate the accuracy of each model and determine the optimal SSC evaluation scheme; and (3) use the optimal evaluation scheme to map the SSC distribution and analyze the spatial patterns of SSC for the arable land in the study area. The results of this study can provide an important reference for timely and accurate soil salinity evaluation.

2. Materials and Methods

2.1. Study Area

The study area is located in the oasis arable land of the Manas River Basin, the southern part of the Junggar Basin, Xinjiang Uyghur Autonomous Region, China ($85^{\circ}8'37''$ – $86^{\circ}23'39''$ E, $44^{\circ}8'48''$ – $44^{\circ}59'37''$ N). The total area covers $5.483 \times 10^3 \text{ km}^2$ at an elevation between 300 and 600 m, and the terrain gradually decreases from southeast to northwest (Figure 1). This region features a typical temperate continental climate characterized by abundant sunshine, low precipitation, and high evaporation rates, with significant temperature variations between day and night. The annual average temperature, precipitation, and evaporation rate are 7.5 – 8.2°C , 180–270 mm, and 1000–1500 mm, respectively. The evaporation rate far exceeds precipitation, creating favorable conditions for soil salinization [34,35]. The main soil types in the study area include calcisol, fluvisol, and gleysol. The land use type is mainly arable land, accounting for 78% of the total area of the study area. The main crop

is cotton, which occupies 85–90% of the total arable land [36,37]. The primary irrigation method is subsurface drip irrigation [38]. Glacier meltwater from mountainous regions is one of the primary water sources for the oasis. As it flows, the meltwater carries salts from rock weathering, which deposit in the soil, exacerbating the salinization of the oasis. As the terrain flattens, the salts the water takes accumulate in the soil, further intensifying salinization [39]. Additionally, during early land reclamation, improper irrigation practices caused the groundwater level to rise. Combined with the high mineralization of irrigation water, this led to secondary salinization in the basin [40]. These issues have not only severely hindered the development of oasis agriculture in arid areas but also present significant challenges for the evaluation and management of soil salinization.

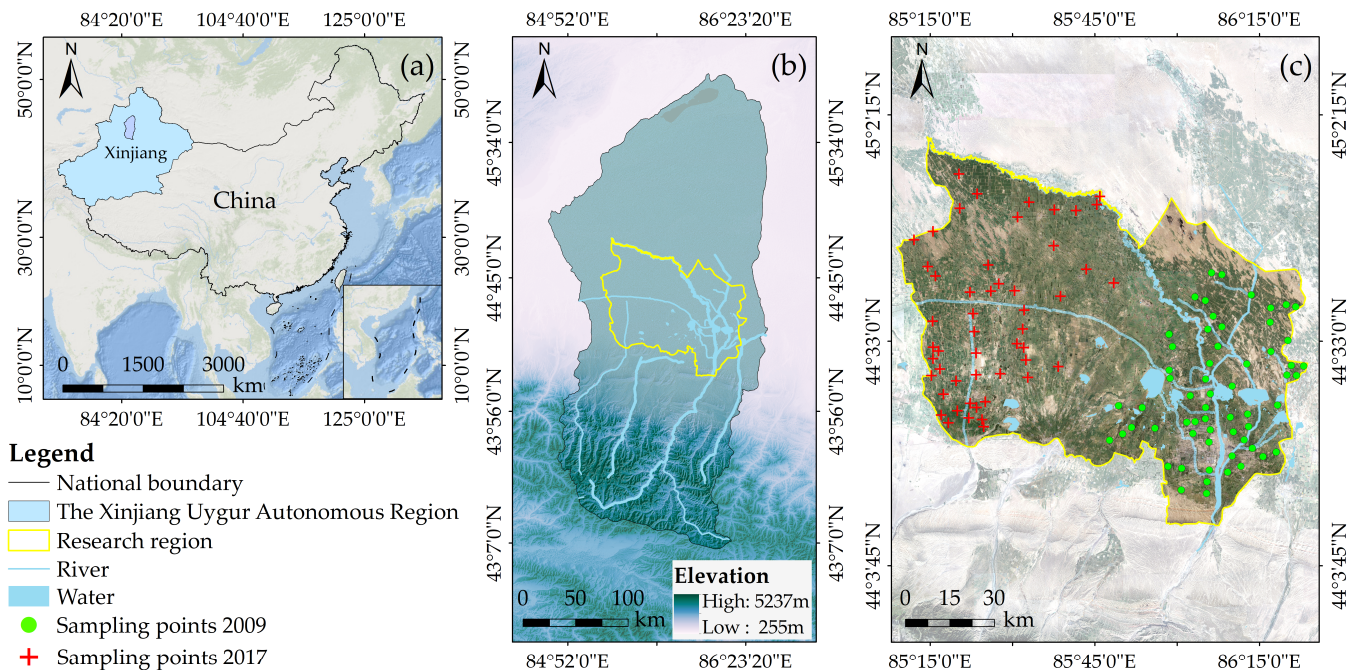


Figure 1. Schematic diagram of the study area: (a) Xinjiang Uygur Autonomous Region, China; (b) elevation of the Manas River Basin; (c) location of sampling points in arable land in the basin.

2.2. Methodological Framework

The methodological framework of this study is depicted in Figure 2 and comprises the following steps: (1) Landsat-5 TM, Landsat-8 OLI, and MCD43A4 images, along with ground data, were collected for the study area. The flexible spatiotemporal data fusion (FSDAF) model was used to fuse the Landsat and MCD43A4 images and obtain fine-resolution fused images synchronized with ground sampling times. This fusion combines Landsat's fine spatial resolution with MODIS's high temporal frequency, addressing both spatial detail and temporal consistency, which are critical for accurate SSC evaluation; (2) the correlation between 14 salinity indices of satellite images was calculated, both synchronized and unsynchronized, with ground sampling times, SSC at a depth of 0–30 cm, and selection of the optimal salinity indices; (3) and the optimal salinity indices were used as input variables, three evaluation models (SVR, RF, and CNN) were constructed based on satellite images, synchronized and unsynchronized, with ground sampling times, the optimal SSC evaluation scheme was selected, and this scheme was used to map the spatial distribution of SSC in the arable land of the study area.

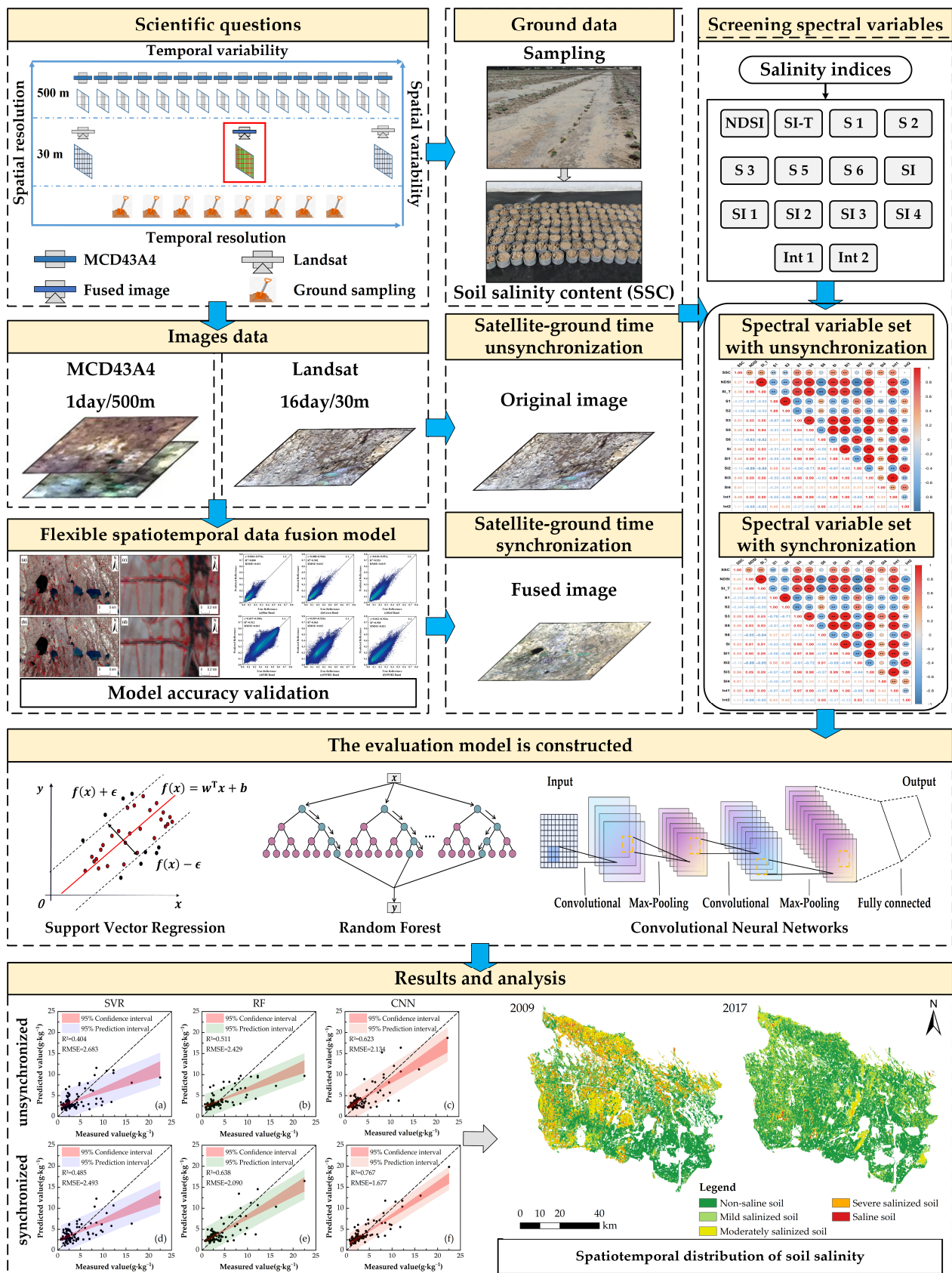


Figure 2. Methodological flowchart.

2.3. Soil Sample Collection and Analysis

Field sampling was conducted from 9 May to 16 May 2009 and from 18 July to 22 July 2017, with 61 and 43 soil samples collected, respectively. In May, during the early growth stage of cotton, precipitation and snowmelt led to salinity accumulation in the surface soil. In July, during the peak growth season, high transpiration and irrigation caused salinity to infiltrate deeper into the soil. This dual-period sampling allowed for a comprehensive analysis of soil salinity fluctuations during key stages of the crop growth cycle. Sampling locations were determined based on the salinization status and uniformity and representativeness of sampling points within the study area. The distance between sampling points was 2–3 km. The sampling method used was the five-point sampling technique. For each sampling point, four replicate samples were taken at approximately 10 m along the diagonals within a 30 m × 30 m area, resulting in five replicates per location. Soil samples were collected from a depth of 0–30 cm using a soil auger, and the latitude and longitude of each sampling point were precisely recorded using GPS.

The soil samples were air-dried, ground, and sieved through a 2 mm mesh. To determine the soil salinity content (SSC), measured in $\text{g}\cdot\text{kg}^{-1}$, soil–water extracts were prepared at a 1:5 ratio following the dry residue method. According to the Xinjiang soil salinization grading standard, soil salinization levels were classified into five categories [41]: non-saline soil ($<3 \text{ g}\cdot\text{kg}^{-1}$), mildly salinized soil ($3\text{--}6 \text{ g}\cdot\text{kg}^{-1}$), moderately salinized soil ($6\text{--}10 \text{ g}\cdot\text{kg}^{-1}$), severely salinized soil ($10\text{--}20 \text{ g}\cdot\text{kg}^{-1}$), and saline soil ($>20 \text{ g}\cdot\text{kg}^{-1}$).

2.4. Satellite Imagery and Preprocessing

In this study, to accurately evaluate surface salinity, factors such as image quality and acquisition dates were comprehensively considered. Landsat-5 TM and Landsat-8 OLI satellite images were sourced from the LANDSAT/LT05/C02/T1_L2 and LANDSAT/LC08/C02/T1_L2 datasets on the Google Earth Engine (GEE) platform. Both datasets provide 30 m surface reflectance and are 16 days composite products [42]. The MODIS satellite images were sourced from the MODIS/006/MCD43A4 dataset, offering daily surface reflectance with a spatial resolution of 500 m [43]. Additionally, the arable land boundaries were extracted using the 30 m resolution GlobeLand30 land cover products from 2010 and 2020 [44]. Detailed information on the satellite images is provided in Table 1.

Table 1. Corresponding information for Landsat-5 TM, Landsat-8 OLI, and MODIS satellite imagery data.

Band Names	Landsat-5 TM Bands	Resolution (m)	Bandwidth (nm)	Landsat-8 OLI Bands	Resolution (m)	Bandwidth (nm)	MCD43A4 Bands	Resolution (m)	Bandwidth (nm)
Blue	1	30	450–520	2	30	452–512	3	500	459–479
Green	2	30	520–600	3	30	533–590	4	500	545–565
Red	3	30	630–690	4	30	636–673	1	500	620–670
NIR	4	30	770–900	5	30	851–879	2	500	841–876
SWIR1	5	30	1550–1750	6	30	1566–1651	6	500	1628–1652
SWIR2	7	30	2080–2350	7	30	2107–2294	7	500	2105–2155

In this study, image preprocessing and downloading were completed using the GEE platform [45]. We analyzed the correlation between SSC and Landsat images before and after ground sampling, as well as the correlation between SSC and MODIS images. Based on this analysis, Landsat-5 TM and MCD43A4 images from 20 May 2009 and Landsat-8 OLI and MCD43A4 images from 13 July 2017 were selected as the base datasets. The MCD43A4 images from 13 May 2009 and 20 July 2017 were used as coarse-resolution images to generate fine-resolution fused images for those dates. The analysis involved six spectral bands: blue, green, red, near-infrared (NIR), shortwave infrared 1 (SWIR1), and shortwave infrared 2 (SWIR2). MODIS images were reprojected and resampled to a 30 m resolution using ENVI 5.3 software to ensure pixel alignment with the Landsat images.

Numerous studies have confirmed that salinity indices are effective indicators for characterizing SSC [21]. This study selected 14 salinity indices closely related to SSC and performed Pearson correlation analysis using R Studio 2022 software. The formulas for these indices are detailed in Table 2.

Table 2. Salinity indices and their calculation formulas.

Salinity Indices	Equation	Reference
NDSI	$(R - NIR) / (R + NIR)$	[46]
SI-T	$(R/NIR) \times 100$	[47]
S1	B / R	[48]
S2	$(B - R) / (B + R)$	[48]
S3	$(G \times R) / B$	[48]
S5	$(B \times R) / G$	[48]
S6	$(R \times NIR) / G$	[48]
SI	$\sqrt{B \times R}$	[46]
SI1	$\sqrt{G \times R}$	[49]
SI2	$\sqrt{G^2 + R^2 + NIR^2}$	[49]
SI3	$\sqrt{G^2 + R^2}$	[49]
SI4	$\sqrt{(B - G)^2 + (G - R)^2}$	[50]
Int1	$(G + R) / 2$	[49]
Int2	$(G + R + NIR) / 2$	[49]

Note: B: blue, G: green, R: red, NIR: near infrared.

2.5. Methods

2.5.1. Spatiotemporal Fusion Method

The spatiotemporal fusion method employs the flexible spatiotemporal data fusion (FSDAF) model proposed by Zhu et al. [51]. This model uses a pair of fine- and coarse-resolution satellite images at time T_a and a coarse-resolution image at time T_b to predict a fine-resolution image at time T_b . The fine-resolution images capture spatial detail changes, while the coarse-resolution images accurately describe temporal changes in features, thereby capturing the spatiotemporal features of the terrain.

2.5.2. Construction of Soil Salinity Evaluation Model

Three different regression methods were used to establish SSC evaluation models, as described below:

Support vector regression (SVR) is a machine learning method based on statistical learning theory that maps data to a high-dimensional feature space through nonlinear transformation to construct the model [26]. SVR is robust in handling small samples and nonlinear data. Random forest (RF) is an ensemble learning method that constructs multiple decision trees and averages their results for prediction [27]. This model excels in handling large datasets and shows high robustness to outliers. A convolutional neural network (CNN) is a deep learning architecture designed to predict continuous values by learning the hierarchical spatial features of input data [33]. This model includes multiple convolutional layers, pooling layers, fully connected layers, and an output layer, demonstrating excellent capability in processing data with spatial correlations.

2.5.3. Model Verification and Accuracy

Validate the Accuracy of the Fusion Model

To evaluate the FSDAF model's effectiveness in fusing spatial and temporal information between different satellite sensors, we selected satellite images from years close to the two sampling periods. These images, which were free from cloud cover or atmospheric interference and aligned with ground sampling dates, were fused to validate the model's accuracy and stability. Specifically, we chose the MCD43A4 image from 15 May 2007, and fused it with Landsat-5 TM and MCD43A4 images from 31 May 2007, to generate

a fine-resolution fused image for 15 May, which was then compared with the original Landsat-5 TM image from the same date. Similarly, we fused the MCD43A4 image from 1 August 2018, with Landsat-8 OLI and MCD43A4 images from 16 July 2018, to create a fine-resolution fused image for 1 August. This fused image was then compared with the original Landsat-8 OLI image to evaluate the model's accuracy and stability.

The stability and predictive accuracy of the fusion model were validated using the coefficient of determination (R^2) and root mean square error (RMSE). R^2 measures the model's fit, while RMSE quantifies the deviation between the fused image and the original image. An R^2 value closer to 1 and a smaller RMSE indicate higher model accuracy and better stability. The expressions for these evaluation metrics are as follows:

$$R^2 = 1 - \frac{\sum_{i=1}^n (y_i - \hat{y}_i)^2}{\sum_{i=1}^n (y_i - \bar{y}_i)^2} \quad (1)$$

$$RMSE = \sqrt{\frac{\sum_{i=1}^n (y_i - \hat{y}_i)^2}{n}} \quad (2)$$

where n is the total number of pixels; y_i is the reflectance of the i -th pixel in the original image; \hat{y}_i is the reflectance of the i -th pixel in the fused image; and \bar{y}_i is the mean reflectance of the original image.

Validate the Accuracy of the Soil Salinity Evaluation Model

To enhance the model's stability, we combined the soil samples from May 2009 and July 2017, resulting in a total dataset of 104 samples with their corresponding salinity indices, which was used to construct the model. First, before building the model, the combined 104 soil samples and their corresponding salinity indices were normalized using the min-max scaling method, standardizing the data to a range of 0 to 1. This ensured that different variables contributed proportionally to the model and reduced potential biases caused by environmental changes and variations in sampling conditions between the two years, thereby improving model stability and convergence [52]. Next, the optimal hyperparameters for each model were identified using a grid search strategy combined with 10-fold cross-validation. This method reduced the risk of overfitting during parameter tuning while maintaining high computational efficiency [53]. It systematically evaluated various hyperparameter combinations to find those that minimized validation errors. In this cross-validation method, the data were divided into 10 equally sized subsets. In each iteration, 9 subsets were used for training, and the remaining subset was used for validation. The results from all 10 iterations were averaged to evaluate each hyperparameter combination's effectiveness. After determining the optimal hyperparameters, the entire dataset was used to train the model and generate predictions. The predicted results were then denormalized to the original scale to ensure interpretability. Finally, the model's performance was evaluated using the leave-one-out cross-validation (LOOCV) method [54]. Specifically, in each iteration, one sample from the combined set was set aside as the validation sample, while the remaining 103 samples were used for training the model. This process was repeated for all 104 samples, with the final performance of the model being assessed by averaging the results from all individual validation iterations. LOOCV is particularly suitable for studies involving small sample sizes, such as ours, as it maximizes the use of all available data while minimizing the uncertainty introduced by arbitrary data partitioning. It also provides a performance evaluation that closely approximates training on the entire dataset, which is essential given the limited number of samples available in this study.

During the selection of optimal hyperparameters for each model, RMSE was used as the evaluation metric. For the final evaluation of model performance, the same metrics as the fusion model were applied, using R^2 and RMSE to evaluate the predictive performance of the models. Where n is the number of sampling points; y_i is the observed value of soil

sample i ; \hat{y}_i is the predicted value of soil sample i ; and \bar{y}_i is the mean observed value of the soil samples.

3. Results

3.1. Statistical Analysis of Soil Salinity Data

Table 3 shows the statistical characteristics of SSC at a depth of 0–30 cm for two different years within the study area. In spring 2009, SSC ranged from 1.25–22.50 g·kg^{−1}, with an average of 4.76 g·kg^{−1}, a median of 2.80 g·kg^{−1}, and a standard deviation of 4.03 g·kg^{−1}. In summer 2017, SSC ranged from 0.68–9.67 g·kg^{−1}, with an average of 2.53 g·kg^{−1}, a median of 1.93 g·kg^{−1}, and a standard deviation of 1.93 g·kg^{−1}. Based on the coefficient of variation (CV), which was below 100% in both years, the SSC showed moderate variability, indicating a relatively uniform spatial distribution of soil salinization in the study area. Additionally, the surface SSC in spring was notably higher than in summer, exhibiting obvious seasonal variation characteristics. This finding aligns with the results of Sun et al. [55], which showed that increased rainfall and frequent irrigation in the arable land during the summer substantially reduce surface salinity levels.

Table 3. Statistical analysis of soil salinity content (g·kg^{−1}) characteristics.

Year	Total Sample	Max	Min	Mean	Median	SD	CV
2009	61	22.50	1.25	4.76	2.80	4.03	84.62%
2017	43	9.67	0.68	2.53	1.93	1.93	76.40%

Note: SD is the standard deviation; CV is the coefficient of variation; n is the number of samples.

3.2. Accuracy Verification of the Fusion Model

The fused and original images of the study area from 15 May 2007, and 1 August 2018, were processed using false-color composition and local magnification (Figure 3). Visual interpretation demonstrates that the fused images generated by the FSDAF model provide clear spatial details and distinct layering, closely resembling the original images. This indicates that the model accurately reconstructs the spatial characteristics and hierarchical information of fine-resolution images for both time periods. The scatter plots of reflectance in each band (Figures 4 and 5) show a strong linear correlation between predicted and true reflectance across all six bands. The FSDAF model performed exceptionally well in both the 2007 and 2018 validations. Notably, the red, NIR, and SWIR2 bands exhibited the highest correlations for both years, with R^2 values of 0.923, 0.912, and 0.930 in 2017, further increasing to 0.941, 0.951, and 0.938 in 2018. The RMSE values for all bands were less than or equal to 0.03. The results indicate that the fused images generated by the FSDAF model are highly similar to the original images across different years and bands, demonstrating the model's high fusion accuracy and stability. This further confirms that the FSDAF model can effectively produce synchronized fine-resolution images, even when satellite imagery and ground sampling times are not aligned. Thus, this study successfully obtained fine-resolution fused images synchronized with the ground sampling times on 13 May 2009, and 20 July 2017, using the FSDAF model.

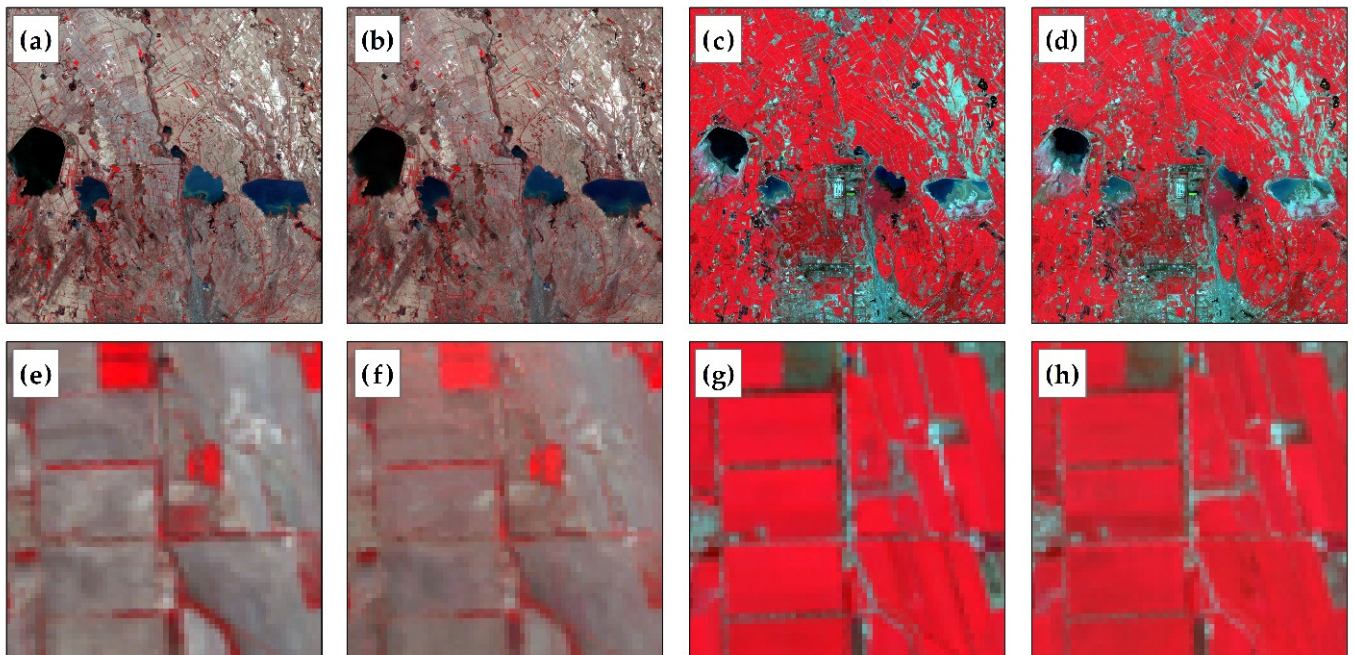


Figure 3. False-color composite comparison between original and fused images for 2007 and 2018: (a,b) Original and fused images (2007); (c,d) Original and fused images (2018); (e,f) Detailed maps of original and fused images (2007); (g,h) Detailed maps of original and fused images (2018).

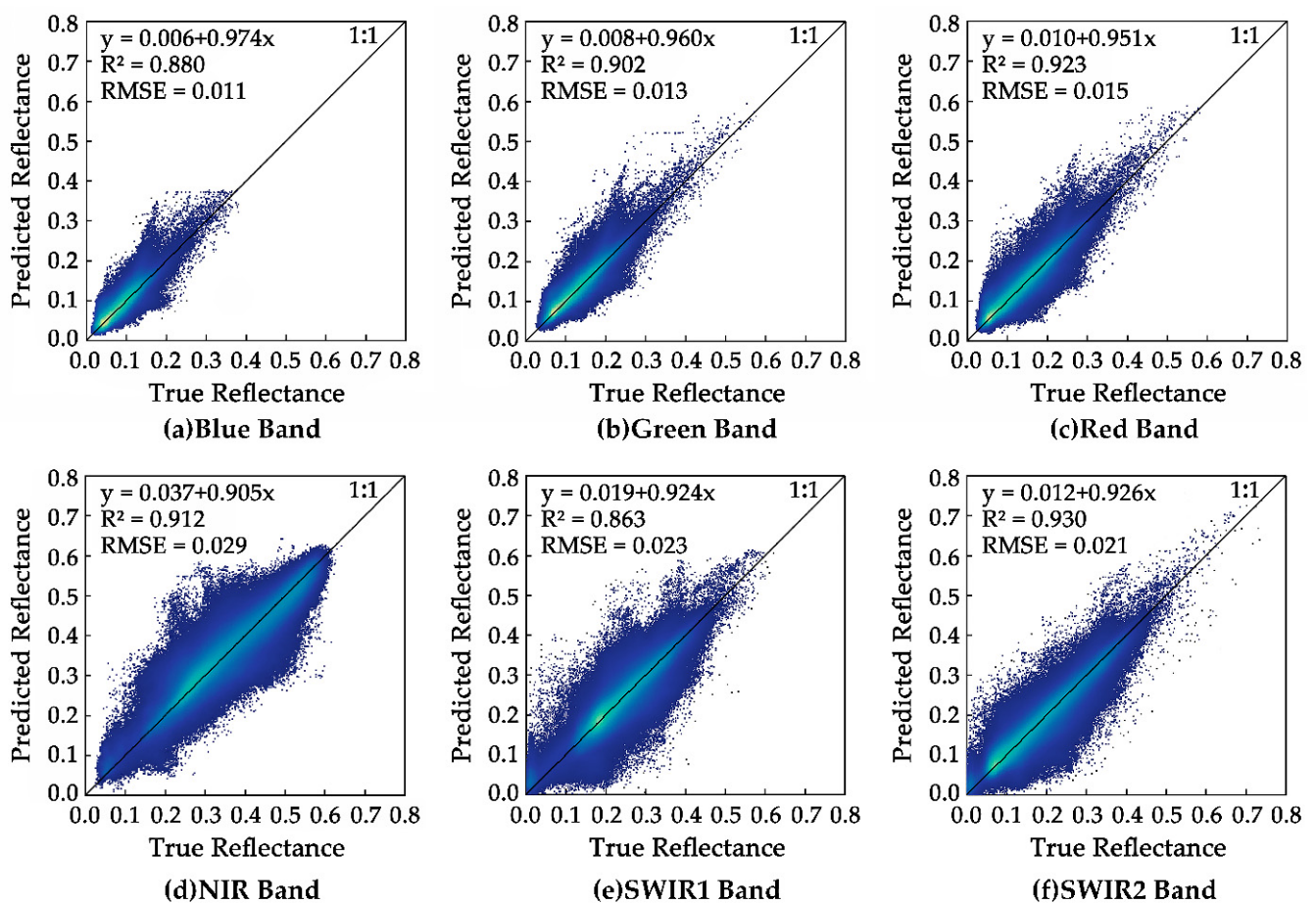


Figure 4. Scatter plots of band reflectance for fused image and original image for 2007: (a) blue band; (b) green band; (c) red band; (d) NIR band; (e) SWIR1 band; (f) SWIR2 band.

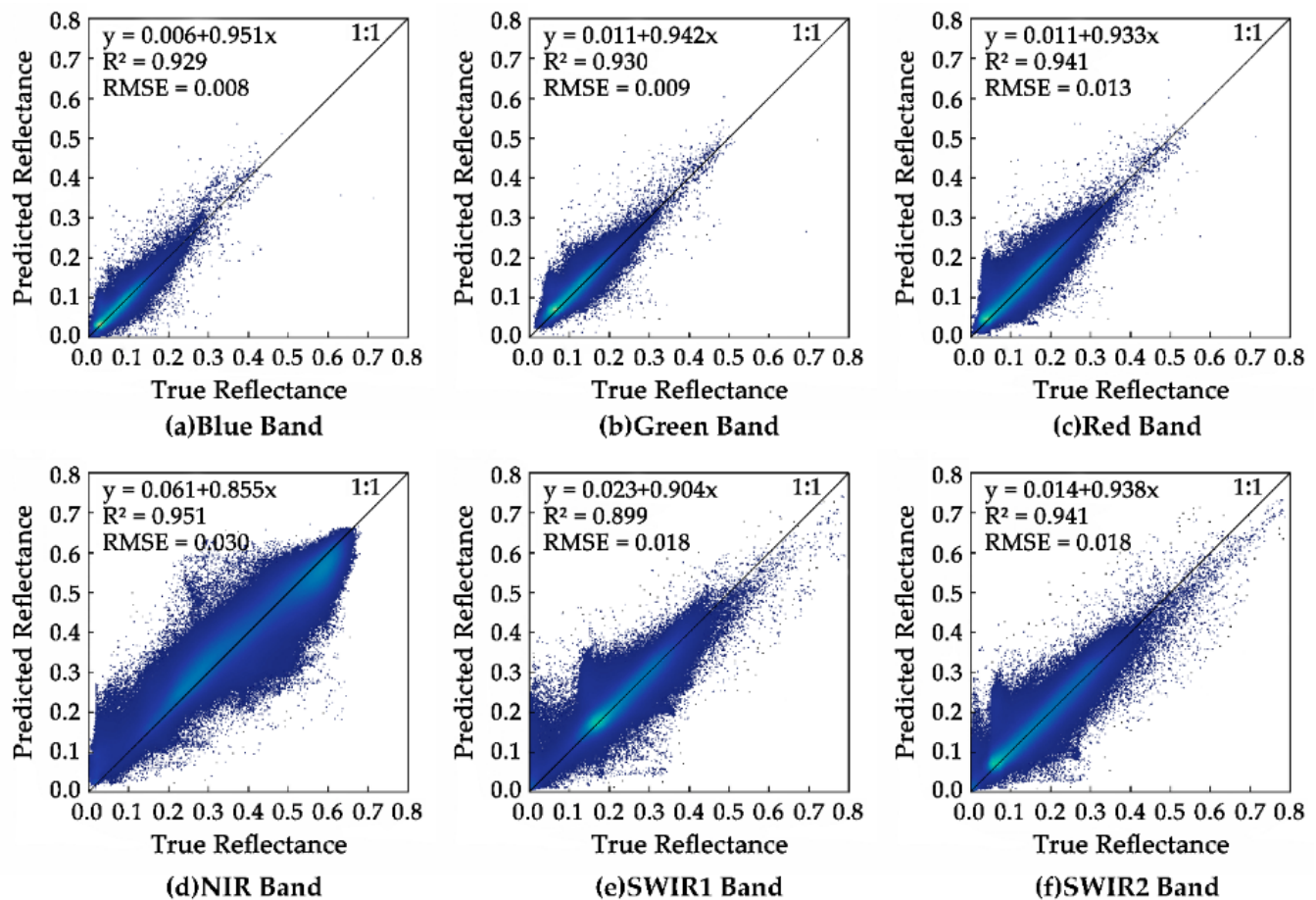
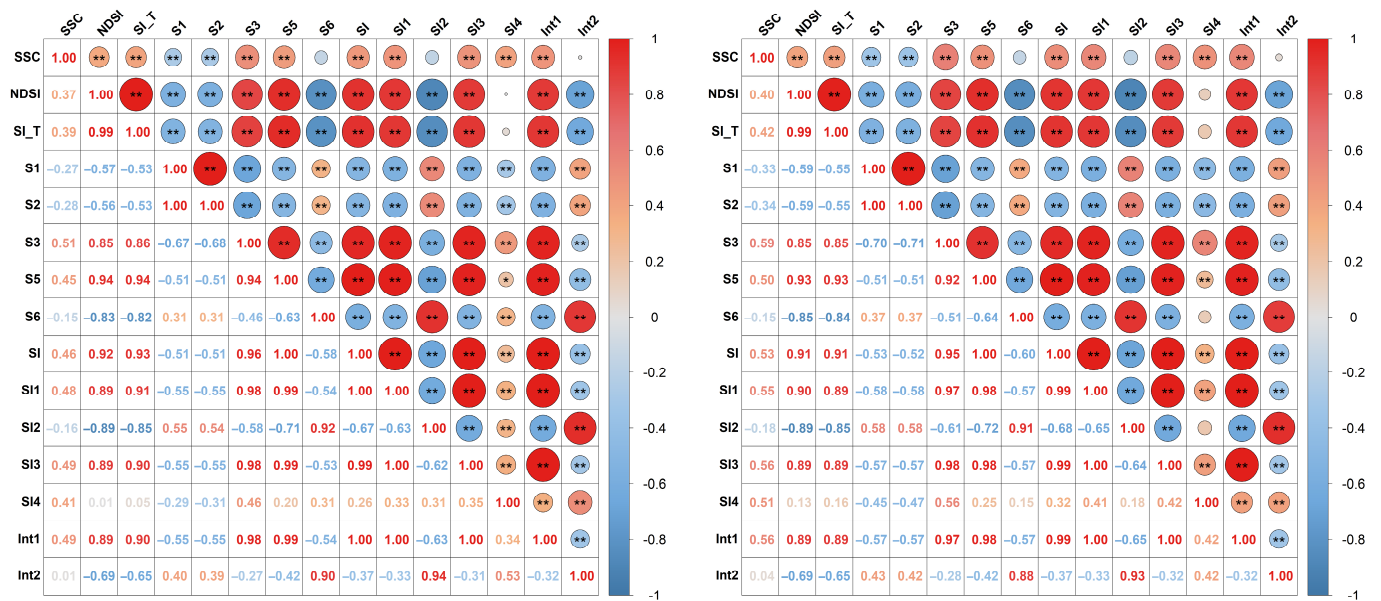


Figure 5. Scatter plots of band reflectance for fused image and original image for 2018: (a) blue band; (b) green band; (c) red band; (d) NIR band; (e) SWIR1 band; (f) SWIR2 band.

3.3. Correlation Analysis

Figure 6 shows the correlation heatmaps comparing the relationships between 14 salinity indices and SSC in satellite images synchronized and unsynchronized with ground sampling times. Overall, the fused images synchronized with ground sampling times exhibit stronger correlations with SSC compared to the original unsynchronized Landsat images. In particular, the salinity indices S3, SI, SI1, SI3, and Int1 show a significant improvement in correlation with SSC when synchronization is applied. These indices had their correlation coefficients (R) increase by more than 0.07 in the synchronized fused images, with S3, SI1, SI3, and Int1 displaying the highest correlations, with R values of 0.59, 0.55, 0.56, and 0.56, respectively. These values are statistically significant at the 0.01 probability level, highlighting the benefit of synchronizing satellite images with ground sampling times for SSC evaluation. Furthermore, additional indices, including NDSI, SI-T, S1, S2, S5, SI, and SI4, in the synchronized images also exhibited statistically significant correlations, with R values ranging from 0.40 to 0.53 (significant at the 0.01 level). In contrast, in the unsynchronized original images, only S3 achieved an R value above 0.5 ($R = 0.51$), while the other salinity indices had weaker correlations, with R values below 0.5. Based on these results, this study selected the seven salinity indices (S3, S5, SI, SI1, SI3, SI4, and Int1) that had R values over 0.5 in the fused image synchronized with ground sampling times and over 0.4 in the original image unsynchronized with ground sampling times as the optimal feature variables for constructing SSC evaluation models, ensuring the models' effectiveness and comparability.



(a)

(b)

Figure 6. Correlation heatmap between salinity indices and soil salinity content: (a) original image; (b) fused image. ** significant at the 0.01 probability level. * significant at the 0.05 probability level.

3.4. Construction and Validation of the Soil Salinity Evaluation Models

3.4.1. Comparison of Accuracy Across Different Evaluation Models

To validate the predictive capability of the three SSC evaluation models in the study area, seven optimal salinity indices were used as input variables, with the combined dataset of 104 field-measured SSC serving as the base dataset. SVR, RF, and CNN models were constructed for both satellite images synchronized and unsynchronized with ground sampling times. The optimal parameters for each model were determined using grid search and 10-fold cross-validation (Table 4).

Table 4. Evaluation model structure.

Model	Image Type	Parameters / Layers	Filter Size	Number of Neurons	Activation Function
SVR	Original image	kernel = RBF, cost = 3, gamma = 0.43, epsilon = 0.05	-	-	-
	Fused image	kernel = RBF, cost = 5, gamma=0.62, epsilon = 0.07	-	-	-
RF	Original image	ntree = 141, mtry = 4	-	-	-
		ntree = 150, mtry = 3	-	-	-
	Fused image	Convolutional layer	3 × 1	16	ReLU
		Max-Pooling layer	2 × 1	-	-
CNN	Original image	Convolutional layer	3 × 1	32	ReLU
		Fully connected layer	-	64	ReLU
		Output layer	-	1	Linear
		Convolutional layer	3 × 1	16	ReLU
	Fused image	Max-Pooling layer	2 × 1	-	-
		Convolutional layer	3 × 1	32	ReLU
		Fully connected layer	-	64	ReLU
		Output layer	-	1	Linear

Table 5 shows the R^2 and RMSE values for each model. The results indicate that the models constructed using fused images synchronized with ground sampling times significantly outperformed those using original images unsynchronized with ground sampling times in terms of predictive accuracy. Compared to the evaluation models based on the

original images unsynchronized with ground sampling, the models using fused images synchronized with ground sampling showed an increase in R^2 values by at least 0.081. This improvement indicates that the FSDAF model effectively addresses temporal mismatches between spectral information and ground measurements, enhancing the accuracy of SSC evaluations. Among the specific models, the RF model showed the most significant improvement, with the R^2 increasing from 0.511 to 0.638, a 24.85% improvement, and the RMSE decreasing from $2.429 \text{ g}\cdot\text{kg}^{-1}$ to $2.090 \text{ g}\cdot\text{kg}^{-1}$. The CNN model followed, with the R^2 increasing from 0.623 to 0.767, a 23.11% improvement, and the RMSE decreasing from $2.134 \text{ g}\cdot\text{kg}^{-1}$ to $1.677 \text{ g}\cdot\text{kg}^{-1}$. The SVR model showed the smallest improvement, with the R^2 increasing from 0.404 to 0.485, a 20.05% improvement, and the RMSE decreasing from $2.683 \text{ g}\cdot\text{kg}^{-1}$ to $2.493 \text{ g}\cdot\text{kg}^{-1}$. Among the three models, the CNN model exhibited the highest predictive accuracy in evaluating SSC, regardless of whether the satellite images were synchronized or unsynchronized with ground sampling times. Therefore, the CNN model is deemed the most suitable for evaluating soil salinity in arid regions, particularly where accurate synchronization with ground sampling times is crucial.

Table 5. Comparison of evaluation model accuracy.

Model	R^2	RMSE ($\text{g}\cdot\text{kg}^{-1}$)
Original image—SVR	0.404	2.683
Fused image—SVR	0.485	2.493
Original image—RF	0.511	2.429
Fused image—RF	0.638	2.090
Original image—CNN	0.623	2.134
Fused image—CNN	0.767	1.677

Figure 7 shows scatter plots comparing observed versus predicted SSC values across the three evaluation models (SVR, RF, and CNN) based on two types of satellite images: synchronized with ground sampling times and unsynchronized. For models using unsynchronized original images, the evaluation models performed well in predicting SSC for non-saline and mildly salinized soils. However, for SSC values exceeding $10 \text{ g}\cdot\text{kg}^{-1}$ in severely salinized soils, all models underestimated the actual observed values, resulting in less satisfactory predictions. In contrast, the models based on synchronized fused images significantly improved the prediction accuracy across the SSC range. The synchronized models performed particularly well for SSC values between $0\text{--}15 \text{ g}\cdot\text{kg}^{-1}$, although slight underestimations occurred for values exceeding $15 \text{ g}\cdot\text{kg}^{-1}$. Among the models, the CNN model demonstrated the highest predictive accuracy, outperforming both the SVR and RF models. For SSC values exceeding $15 \text{ g}\cdot\text{kg}^{-1}$, the CNN model's predictions were closer to the 1:1 line compared to the other models. In summary, the combination of the CNN model with fused images synchronized with ground sampling times provides the most reliable SSC evaluation, making it the optimal scheme for evaluating soil salinity in arid regions.

3.4.2. Spatiotemporal Analysis of Soil Salinity Content

This study used the optimal evaluation scheme, the CNN model based on fused images synchronized with ground sampling times, to map the spatiotemporal distribution of SSC in the Manas River Basin's arable land for May 2009 and July 2017. The spatial and temporal changes in soil salinity levels are shown in Figure 8. In terms of spatial distribution, the soil salinization level in the study area during the spring of 2009 showed a pattern of lower salinization in the southeast and higher salinization in the northwest. Non-saline soil was mainly distributed in the southeastern part of the study area, while mildly and moderately salinized soils were concentrated in the central region. Severely salinized soil and saline soil were primarily found in the northwestern and northern edges of the arable land. By the summer of 2017, there was a clear improvement in soil salinization levels. The areas of non-saline soil and mildly salinized soil increased, while the severely

salinized and saline soils in the northern and northwestern regions showed significant reductions. This may be attributed to the fact that, in spring, soil is often affected by precipitation and snowmelt, which can transport salts to the surface, resulting in higher levels of salinization. In summer, although high temperatures and evaporation might have intensified salt accumulation, crop growth and transpiration effectively reduced salt concentrations on the soil surface. Additionally, increased irrigation activities caused salts to move to deeper soil layers, further reducing surface soil salinity. Overall, the level of soil salinization in this region was relatively low, and the evaluation results were consistent with field surveys.

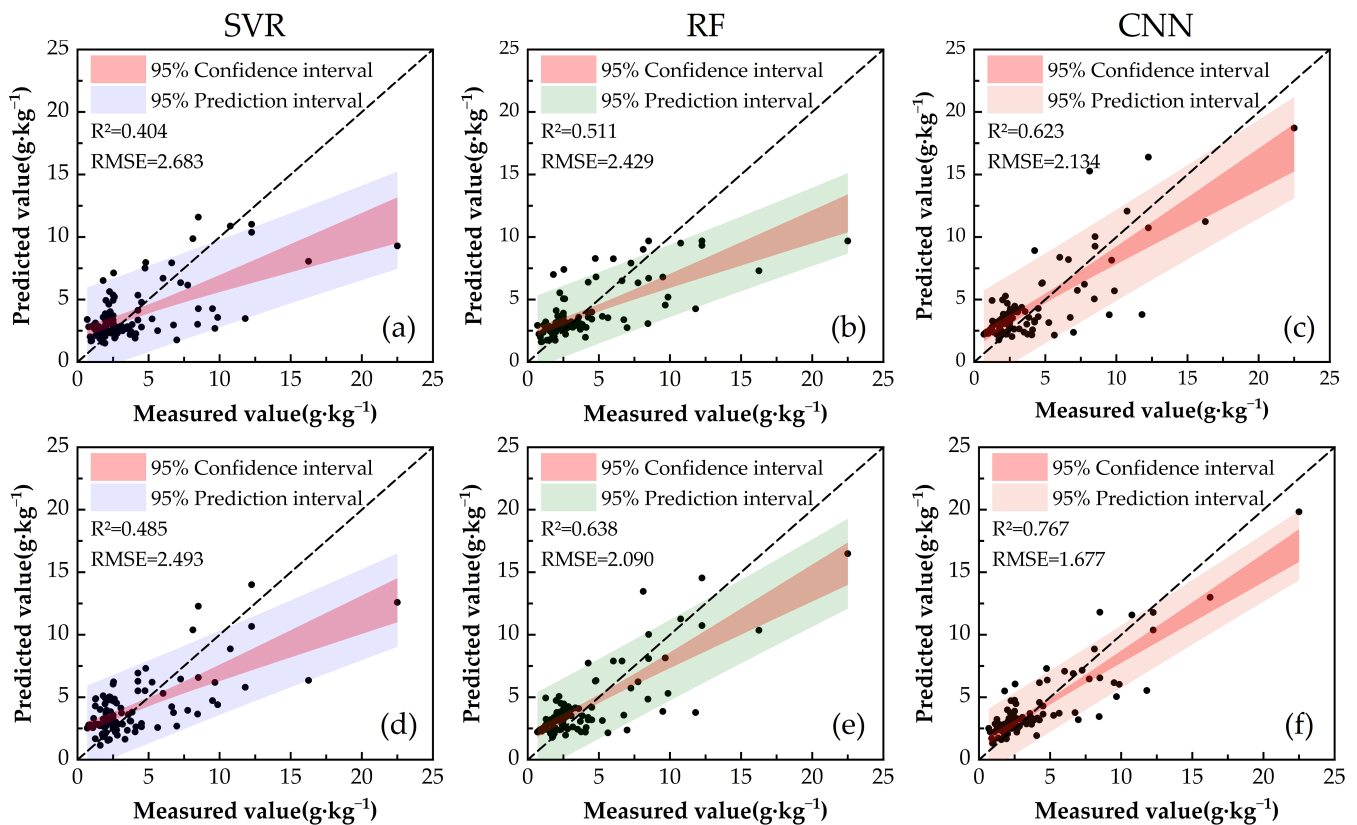


Figure 7. Scatter plot of observed versus predicted values by the model: (a) original image—SVR model; (b) original image—RF model; (c) original image—CNN model; (d) fused image—SVR model; (e) fused image—RF model; (f) fused image—CNN model.

Table 6 shows that from 2009 to 2017, 1083.26 km² of non-saline soil remained in its non-saline state, representing the vast majority of this type. The remaining area mostly transformed into mildly salinized soil, with smaller portions transitioning to moderately salinized, severely salinized, and saline soil, covering 467.33 km², 138.28 km², 8.69 km², and 7.87 km², respectively. Mildly salinized soil transitioned to non-saline soil, moderately salinized soil, severely salinized soil, and saline soil, covering areas of 489.22 km², 287.53 km², 73.31 km², and 7.07 km², respectively. Moderately salinized soil converted to non-saline soil, mildly salinized soil, severely salinized soil, and saline soil over areas of 415.09 km², 187.15 km², 47.54 km², and 4.32 km², respectively. Severely salinized soil transitioned to non-saline soil, mildly salinized soil, moderately salinized soil, and saline soil, covering 252.12 km², 111.86 km², 28.80 km², and 1.60 km², respectively. Saline soil converted to non-saline soil, mildly salinized soil, moderately salinized soil, and severely salinized soil over areas of 91.65 km², 48.98 km², 11.97 km², and 0.66 km², respectively. Overall, soil salinization in the study area improved in 2017, with significant recovery observed in areas affected by mild to moderate salinization. However, some areas have experienced worsening soil salinization, especially the transition from mildly salinized soil

to higher salinization levels, which may be linked to poor local water management, climate change, or other external factors. Therefore, despite the overall positive trend, continuous management of key salinization areas is necessary to prevent further deterioration of the salinization problem.

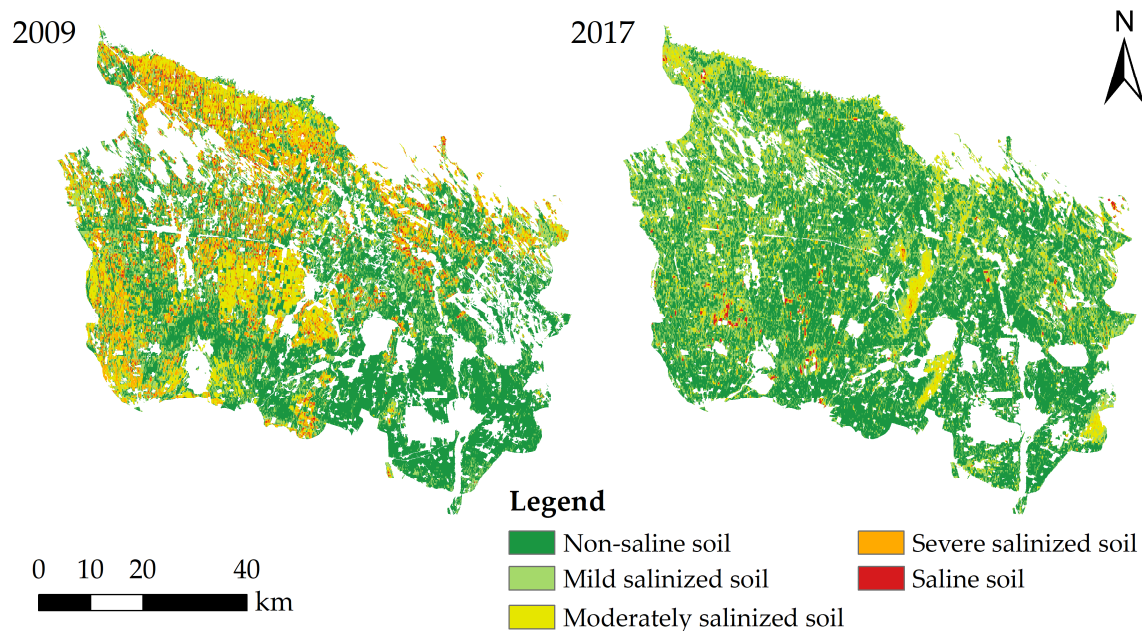


Figure 8. Spatiotemporal distribution of soil salinity based on the optimal evaluation model.

Table 6. Transfer matrix of soil salinization level at 0–30 cm depth for 2009–2017 (km²).

Soil Salinization Level	2017 Non-Saline Soil	2017 Mildly Salinized Soil	2017 Moderately Salinized Soil	2017 Severe Salinized Soil	2017 Saline Soil
2009 Non-saline Soil	1083.26	467.33	138.28	8.69	7.87
2009 Mildly Salinized Soil	489.22	287.53	73.31	4.73	7.07
2009 Moderately Salinized Soil	415.09	187.15	47.54	3.23	4.32
2009 Severe Salinized Soil	252.12	111.86	28.80	1.64	1.60
2009 Saline Soil	91.65	48.98	11.97	0.68	0.66

4. Discussion

4.1. Interpretability and Limitations of Fusion Results

In practical applications, factors such as weather conditions, cloud cover, and imaging intervals can significantly affect the quality and availability of satellite images, often resulting in images that are insufficient for analysis. To address the issue of missing images, spatiotemporal fusion algorithms are used to generate fine-resolution satellite images [14]. This study applied the FSDAF model to fuse satellite images with different temporal and spatial resolutions, obtaining fine-resolution images synchronized with sampling times. This process provided the data foundation for dynamic soil salinization assessment. Visual interpretation and accuracy validation of the fused image confirmed the effectiveness of the FSDAF model in compensating for missing fine-resolution images. The FSDAF model requires only one set of fine- and coarse-resolution images and a coarse-resolution image at the fusion time for image fusion, enhancing its practicality [51]. The FSDAF model's advantage lies in its ability to simulate the evolution of spectral features over different time periods, not merely through simple interpolation but based on spectral transition predic-

tions [56]. This method allows the model to robustly handle spatiotemporal changes in land cover, overcoming the limitations of excessive data requirements and enabling rapid and accurate reconstruction of complex dynamic processes [57,58]. Currently, spatiotemporal fusion techniques mainly include five methods: pixel unmixing-based, weight function-based, dictionary learning-based, Bayesian-based, and multiple hybrid methods [59]. This study applied the FSDAF model, a multiple hybrid method, to the oasis farmland in the Manas River Basin and conducted multi-level validation of its fused images. However, slight differences in fusion accuracy among different methods may impact the accuracy of SSC evaluating results. Therefore, in future research, we will compare various spatiotemporal fusion models and explore improvements to enhance the accuracy of fusion results.

4.2. Comparison of Different Evaluation Models

In this study, we constructed evaluation models using SVR, RF, and CNN, and the results showed that the CNN model consistently outperformed both SVR and RF models in terms of accuracy, particularly in evaluating high-salinity samples. For example, Wang et al. [32] demonstrated that CNN models significantly improved prediction accuracy ($R^2 = 0.79$, $RMSE = 9.41 \text{ g} \cdot \text{kg}^{-1}$) over traditional machine learning methods. Our results align with these findings, as the CNN model showed higher accuracy with fewer errors when applied to satellite images, both synchronized and unsynchronized with ground sampling times. The superior performance of CNN is due to its ability to capture complex nonlinear relationships between spectral features and soil salinity content (SSC) through convolutional layers, making it especially suitable for remote sensing data [33]. In contrast, SVR relies on kernel functions for nonlinear modeling, which limits its generalization ability when processing high-dimensional data like satellite images [26]. Similarly, RF models face challenges due to high correlation among decision trees, reducing model diversity and robustness in spatially complex environments [60]. However, it is important to note that a significant limitation of this study is the small sample size, which may negatively impact the stability of model training and its ability to generalize across different salinity levels. In particular, during the development of deep learning models, the adequacy of sample size directly influences model performance, often leading to overfitting. This results in excellent performance on the training set but poor performance during testing or real-world applications. Nonetheless, a small sample size does not necessarily invalidate the results. Numerous studies have proposed various methods to address small sample challenges. Tan et al. [61], based on 84 ground-truth soil salinity data and various spectral parameters, applied variable selection methods and machine learning algorithms to successfully estimate soil salinity and generate salinity maps. The model achieved an R^2 of 0.832, demonstrating strong predictive performance. Shu et al. [62] compared different sample size combinations and found that, even with a small sample size, accurate models and reliable estimation results can still be achieved by using appropriate modeling methods. In this study, the leave-one-out cross-validation (LOOCV) method was used to address the challenges of limited sample size. LOOCV is particularly suitable for small datasets, as it maximizes data utilization by using each sample as both training and validation data [54]. This technique helps reduce overfitting and ensures a more robust evaluation of model performance, which is crucial when data are limited [63]. Despite the advantages of LOOCV, small sample sizes can still introduce localized biases, as the data may not capture the full variability of soil salinity across the study area. Future research should aim to increase sample size and explore hybrid models that integrate CNN with other techniques to enhance predictive accuracy and generalizability.

4.3. Analysis of the Spatiotemporal Changes of Soil Salinization and Its Influencing Factors

From 2009 to 2017, the soil salinization levels in the Manas River Basin's arable land underwent significant changes. In 2009, SSC measurements were taken during the spring, when salinization was primarily driven by precipitation and snowmelt. These factors facilitated the upward movement of salts from deeper layers to the surface, resulting

in elevated surface salinity levels. By contrast, the 2017 measurements were conducted in the summer, a period characterized by higher temperatures, active crop growth, and frequent irrigation. These conditions enhanced soil water movement through increased transpiration, promoting the leaching of salts from the surface to deeper soil layers and consequently lowering surface salinity. This seasonal shift in soil salinization is consistent with findings by Hao et al. [64]. Overall, from 2009 to 2017, the soil salinization in the arable land improved. The area of non-saline soils increased significantly, and mildly salinized soils expanded. Salinized and saline soils gradually converted to less saline or non-saline categories, indicating effective soil remediation. This improvement was largely attributed to the widespread adoption of water-saving technologies, particularly precision irrigation techniques like subsurface drip irrigation [38]. These techniques, widely applied in the oasis arable land, helped reduce salt accumulation by minimizing water loss and improving irrigation efficiency, leading to better soil quality. However, despite these improvements, salinization worsened in some areas, where non-saline soils were converted into saline soils. This phenomenon may be closely linked to the expansion of the oasis and agricultural land, increasing the demand for water, especially in the arid region. The expansion of the oasis and the growing irrigation needs exacerbated water shortages, limiting effective irrigation management and leading to localized salt accumulation in the soil [40]. Therefore, to prevent further soil salinization, it is essential to enhance water resource management, optimize irrigation techniques, and carefully plan land use to ensure the long-term sustainability of agriculture and the environment in the Manas River Basin.

5. Conclusions

This study proposed a framework for integrated spatiotemporal data fusion and CNN algorithms for evaluating soil salinity, which improves the accuracy of soil salinity evaluation. By combining the FSDAF algorithm with three models (SVR, RF, and CNN), the feasibility and applicability of this framework in the evaluation of soil salinity of arable land in arid areas were validated. The results are as follows:

- (1) The FSDAF model demonstrates high fusion accuracy and can reliably generate fine-resolution images synchronized with ground sampling, even when the satellite imagery and ground sampling dates do not match.
- (2) Synchronizing satellite imagery with ground sampling times significantly improves the accuracy of SSC evaluation. Among the salinity indices, S3, S5, SI, SI1, SI3, SI4, and Int1 exhibited the highest correlations, making them the optimal feature variables for constructing robust and effective SSC evaluation models.
- (3) The CNN model outperformed the RF and SVR models in accuracy, and the evaluation scheme combining fused images synchronized with ground sampling times with the CNN model significantly improved the prediction accuracy of SSC ($R^2 = 0.767$, $RMSE = 1.677 \text{ g} \cdot \text{kg}^{-1}$). Additionally, the overall soil salinization in the study area improved between spring 2009 and summer 2017, though some areas experienced worsening salinization. Therefore, continued management of key areas is necessary to prevent further deterioration of salinization.

In summary, this study combines the temporal and spectral features of satellite images with the advantages of deep learning algorithms, significantly improving the accuracy of SSC evaluation. The results provide a valuable reference for the real-time, rapid, and accurate evaluation of soil salinity of arable land in arid areas.

Author Contributions: Conceptualization, X.W., T.S., J.S. and P.J.; methodology, X.W., J.S. and P.J.; software, T.S. and Z.Z.; validation, T.S., J.S. and H.C.; formal analysis, P.J.; investigation, Q.Y.; resources, X.W.; data curation, S.G.; writing—original draft preparation, T.S.; writing—review and editing, X.W., S.N., J.S. and P.J.; visualization, T.S. and Z.L.; supervision, X.W. and P.J.; project administration, X.W.; funding acquisition, J.S. All authors have read and agreed to the published version of the manuscript.

Funding: This research was funded by the National Key Research and Development Program of China (2021YFD1900801) and Science and Technology Major Project of Xinjiang Uygur Autonomous Region (2023A02002-2).

Data Availability Statement: The data presented in this study are available on request from the corresponding author.

Acknowledgments: We want to thank the editor and anonymous reviewers for their valuable comments and suggestions for this paper.

Conflicts of Interest: The authors declare no conflicts of interest.

References

1. Thaker, P.; Brahmabhatt, N.; Shah, K. Review impact of soil salinity on ecological, agriculture and socioeconomic concerns. *Int. J. Adv. Res.* **2021**, *9*, 979–986. [[CrossRef](#)] [[PubMed](#)]
2. Soni, P.G.; Basak, N.; Rai, A.K.; Sundha, P.; Narjary, B.; Kumar, P.; Yadav, G.; Kumar, S.; Yadav, R.K. Deficit saline water irrigation under reduced tillage and residue mulch improves soil health in sorghum-wheat cropping system in semi-arid region. *Sci. Rep.* **2021**, *11*, 1880. [[CrossRef](#)] [[PubMed](#)]
3. Wang, Y.; Wang, S.; Zhao, Z.; Zhang, K.; Tian, C.; Mai, W. Progress of Euhalophyte Adaptation to Arid Areas to Remediate Salinized Soil. *Agriculture* **2023**, *13*, 704. [[CrossRef](#)]
4. Du, Z.; Gao, B.; Ou, C.; Du, Z.; Yang, J.; Batsaikhan, B.; Dorjgotov, B.; Yun, W.; Zhu, D. A quantitative analysis of factors influencing organic matter concentration in the topsoil of black soil in northeast China based on spatial heterogeneous patterns. *ISPRS Int. J. Geo-Inf.* **2021**, *10*, 348. [[CrossRef](#)]
5. Gorji, T.; Tanik, A.; Sertel, E. Soil salinity prediction, monitoring and mapping using modern technologies. *Procedia Earth Planet. Sci.* **2015**, *15*, 507–512. [[CrossRef](#)]
6. Azabdaftari, A.; Sunar, F. Soil salinity mapping using multitemporal Landsat data. *Int. Arch. Photogramm. Remote Sens. Spat. Inf. Sci.* **2016**, *41*, 3–9. [[CrossRef](#)]
7. Zhang, T.T.; Qi, J.G.; Gao, Y.; Ouyang, Z.T.; Zeng, S.L.; Zhao, B. Detecting soil salinity with MODIS time series VI data. *Ecol. Indic.* **2015**, *52*, 480–489. [[CrossRef](#)]
8. Lobell, D.B.; Lesch, S.M.; Corwin, D.; Ulmer, M.G.; Anderson, K.A.; Potts, D.J.; Doolittle, J.A.; Matos, M.R.; Baltes, M.J. Regional-scale Assessment of Soil Salinity in the Red River Valley Using Multi-year MODIS EVI and NDVI. *J. Environ. Qual.* **2010**, *39*, 35–41. [[CrossRef](#)]
9. Scudiero, E.; Skaggs, T.H.; Corwin, D.L. Regional scale soil salinity evaluation using Landsat 7, western San Joaquin Valley, California, USA. *Geoderma Reg.* **2014**, *2–3*, 82–90. [[CrossRef](#)]
10. Whitney, K.; Scudiero, E.; El-Askary, H.M.; Skaggs, T.H.; Allali, M.; Corwin, D.L. Validating the use of MODIS time series for salinity assessment over agricultural soils in California, USA. *Ecol. Indic.* **2018**, *93*, 889–898. [[CrossRef](#)]
11. Sahbeni, G. Soil salinity mapping using Landsat 8 OLI data and regression modeling in the Great Hungarian Plain. *SN Appl. Sci.* **2021**, *3*, 587. [[CrossRef](#)]
12. Yang, N.; Yang, S.; Cui, W.; Zhang, Z.; Zhang, J.; Chen, J.; Ma, Y.; Lao, C.; Song, Z.; Chen, Y. Effect of spring irrigation on soil salinity monitoring with UAV-borne multispectral sensor. *Int. J. Remote Sens.* **2021**, *42*, 8952–8978. [[CrossRef](#)]
13. Wang, J.Z.; Ding, J.L.; Yu, D.L.; Teng, D.X.; He, B.; Chen, X.Y.; Ge, X.Y.; Zhang, Z.P.; Wang, Y.; Yang, X.D.; et al. Machine learning-based detection of soil salinity in an arid desert region, Northwest China: A comparison between Landsat-8 OLI and Sentinel-2 MSI. *Sci. Total Environ.* **2020**, *707*, 136092. [[CrossRef](#)] [[PubMed](#)]
14. Qi, G.; Chang, C.; Yang, W.; Zhao, G. Soil salinity inversion in coastal cotton growing areas: An integration method using satellite-ground spectral fusion and satellite-UAV collaboration. *Land Degrad. Dev.* **2022**, *33*, 2289–2302. [[CrossRef](#)]
15. Zhao, Q.; Ding, J.; Han, L.; Jin, X.; Hao, J. Exploring the application of MODIS and Landsat spatiotemporal fusion images in soil salinization: A case of Ugan River-Kuqa River Delta Oasis. *Arid. Land Geogr.* **2022**, *45*, 1155–1164.
16. Guo, D.; Shi, W.; Hao, M.; Zhu, X. FSDAF 2.0: Improving the performance of retrieving land cover changes and preserving spatial details. *Remote Sens. Environ.* **2020**, *248*, 111973. [[CrossRef](#)]
17. Han, L.; Ding, J.; Ge, X.; He, B.; Wang, J.; Xie, B.; Zhang, Z. Using spatiotemporal fusion algorithms to fill in potentially absent satellite images for calculating soil salinity: A feasibility study. *Int. J. Appl. Earth Obs. Geoinf.* **2022**, *111*, 102839. [[CrossRef](#)]
18. Allbed, A.; Kumar, L. Soil salinity mapping and monitoring in arid and semi-arid regions using remote sensing technology: A review. *Adv. Remote Sens.* **2013**, *2*, 373–385. [[CrossRef](#)]
19. Zarei, A.; Hasanlou, M.; Mahdianpari, M. A comparison of machine learning models for soil salinity estimation using multi-spectral earth observation data. *Remote Sens. Spat. Inf. Sci.* **2021**, *3*, 257–263. [[CrossRef](#)]
20. Teshaev, N.; Mamadaliyev, B.; Ibragimov, A.; Khasanov, S. The soil-adjusted vegetation index for soil salinity assessment in Uzbekistan. *ICIGIS* **2020**, *26*, 324–333. [[CrossRef](#)]
21. Khan, N.M.; Rastoskuev, V.V.; Sato, Y.; Shiozawa, S. Assessment of hydrosaline land degradation by using a simple approach of remote sensing indicators. *Agric. Water Manag.* **2005**, *77*, 96–109. [[CrossRef](#)]

22. Bouaziz, M.; Matschullat, J.; Gloaguen, R. Improved remote sensing detection of soil salinity from a semi-arid climate in Northeast Brazil. *Comptes Rendus Geosci.* **2011**, *343*, 795–803. [\[CrossRef\]](#)
23. Wang, Q.; Li, P.; Chen, X. Retrieval of soil salt content from an integrated approach of combining inversed reflectance model and regressions: An experimental study. *IEEE Trans. Geosci. Remote Sens.* **2012**, *50*, 3950–3957. [\[CrossRef\]](#)
24. Chen, Y.; Qiu, Y.; Zhang, Z.; Zhang, J.; Chen, C.; Han, J.; Liu, D. Estimating salt content of vegetated soil at different depths with Sentinel-2 data. *Peer J.* **2020**, *8*, e10585. [\[CrossRef\]](#) [\[PubMed\]](#)
25. Lei, G.; Zeng, W.; Yu, J.; Huang, J. A comparison of physical-based and machine learning modeling for soil salt dynamics in crop fields. *Agric. Water Manag.* **2023**, *277*, 108115. [\[CrossRef\]](#)
26. Awad, M.; Khanna, R. Support vector regression. In *Efficient Learning Machines*; Awad, M., Khanna, R., Eds.; Apress: Berkeley, CA, USA, 2015; pp. 67–80. ISBN 978-143-025-990-9.
27. Belgiu, M.; Drăguț, L. Random forest in remote sensing: A review of applications and future directions. *ISPRS J. Photogramm. Remote Sens.* **2016**, *114*, 24–31. [\[CrossRef\]](#)
28. Chen, H.; Zhao, G.; Chen, J.; Wang, R.; Gao, M. Remote sensing inversion of saline soil salinity based on modified vegetation index in estuary area of Yellow River. *Trans. Chin. Soc. Agric. Eng.* **2015**, *31*, 107–114.
29. Fathizad, H.; Ali, H.A.M.; Sodaiezhadeh, H.; Kerry, R.; Taghizadeh-Mehrjardi, R. Investigation of the spatial and temporal variation of soil salinity using random forests in the central desert of Iran. *Geoderma* **2020**, *365*, 114233. [\[CrossRef\]](#)
30. De Gregorio, L.; Callegari, M.; Mazzoli, P.; Bagli, S.; Broccoli, D.; Pistocchi, A.; Notarnicola, C. Operational river discharge forecasting with support vector regression technique applied to alpine catchments: Results, advantages, limits and lesson learned. *Water Resour. Manag.* **2018**, *32*, 229–242. [\[CrossRef\]](#)
31. Schulz, K.; Hänsch, R.; Sörgel, U. Machine learning methods for remote sensing applications: An overview. *Earth Resour. Environ. Remote. Sens./GIS Appl. IX* **2018**, 10790, 1079002.
32. Wang, Y.; Xie, M.; Hu, B.; Jiang, Q.; Shi, Z.; He, Y.; Peng, J. Desert Soil Salinity Inversion Models Based on Field In Situ Spectroscopy in Southern Xinjiang, China. *Remote Sens.* **2022**, *14*, 4962. [\[CrossRef\]](#)
33. Aghdam, H.H.; Heravi, E.J. *Guide to Convolutional Neural Networks*; Springer: New York, NY, USA, 2017; Volume 10.
34. Tuzheng, C.; Li, Y.; Fadong, L.; Xinlin, H. Spatial variability of soil moisture, salinity, and nutrients in cotton fields of different oasis ecosystems in the Manas River basin. *J. Agric. Resour. Environ.* **2022**, *39*, 1133.
35. Ning, S.; Shi, J.; Zuo, Q.; Wang, S.; Ben-Gal, A. Generalization of the root length density distribution of cotton under film mulched drip irrigation. *Field Crops Res.* **2015**, *177*, 125–136. [\[CrossRef\]](#)
36. Ling, H.; Xu, H.; Fu, J.; Fan, Z.; Xu, X. Suitable oasis scale in a typical continental river basin in an arid region of China: A case study of the Manas River Basin. *Quat. Int.* **2013**, *286*, 116–125. [\[CrossRef\]](#)
37. Ning, S.; Zhou, B.; Shi, J.; Wang, Q. Soil water/salt balance and water productivity of typical irrigation schedules for cotton under film mulched drip irrigation in northern Xinjiang. *Agric. Water Manag.* **2021**, *245*, 106651. [\[CrossRef\]](#)
38. Qiao, X.; Yang, G.; Shi, J.; Zuo, Q.; Liu, L.; Niu, M.; Wu, X.; Ben-Gal, A. Remote Sensing Data Fusion to Evaluate Patterns of Regional Evapotranspiration: A Case Study for Dynamics of Film-Mulched Drip-Irrigated Cotton in China's Manas River Basin over 20 Years. *Remote Sens.* **2022**, *14*, 3438. [\[CrossRef\]](#)
39. Yang, G.; Li, F.; Chen, D.; He, X.; Xue, L.; Long, A. Assessment of changes in oasis scale and water management in the arid Manas River Basin, north western China. *Sci. Total Environ.* **2019**, *691*, 506–515. [\[CrossRef\]](#)
40. Zhang, Q.; Xu, H.; Li, Y.; Fan, Z.; Zhang, P.; Yu, P.; Ling, H. Oasis evolution and water resource utilization of a typical area in the inland river basin of an arid area: A case study of the Manas River valley. *Remote Sens. Appl. Soc. Environ.* **2019**, *13*, 415–425. [\[CrossRef\]](#)
41. Wang, L.; Hu, P.; Zheng, H.; Liu, Y.; Cao, X.; Hellwich, O.; Liu, T.; Luo, G.; Bao, A.; Chen, X. Integrative modeling of heterogeneous soil salinity using sparse ground samples and remote sensing images. *Geoderma* **2023**, *430*, 116321. [\[CrossRef\]](#)
42. Chander, G.; Markham, B. Revised Landsat-5 TM radiometric calibration procedures and postcalibration dynamic ranges. *IEEE Trans. Geosci. Remote Sens.* **2003**, *41*, 2674–2677. [\[CrossRef\]](#)
43. Wang, Z.; Schaaf, C.B.; Sun, Q.; Shuai, Y.; Román, M.O. Capturing rapid land surface dynamics with Collection V006 MODIS BRDF/NBAR/Albedo (MCD43) products. *Remote Sens. Environ.* **2018**, *207*, 50–64. [\[CrossRef\]](#)
44. Chen, J.; Chen, J.; Liao, A.; Cao, X.; Chen, L.; Chen, X.; He, C.; Han, G.; Peng, S.; Lu, M. Global land cover mapping at 30 m resolution: A POK-based operational approach. *ISPRS J. Photogramm. Remote Sens.* **2015**, *103*, 7–27. [\[CrossRef\]](#)
45. Amani, M.; Ghorbanian, A.; Ahmadi, S.A.; Kakooei, M.; Moghimi, A.; Mirmazloumi, S.M.; Moghaddam, S.H.A.; Mahdavi, S.; Ghahremanloo, M.; Parsian, S.; et al. Google earth engine cloud computing platform for remote sensing big data applications: A comprehensive review. *IEEE J. Sel. Top. Appl. Earth Observ. Remote Sens.* **2020**, *13*, 5326–5350. [\[CrossRef\]](#)
46. Abuelgasim, A.; Ammad, R. Mapping soil salinity in arid and semi-arid regions using Landsat 8 OLI satellite data. *Remote Sens. Appl. Soc. Environ.* **2019**, *13*, 415–425. [\[CrossRef\]](#)
47. Tripathi, N.; Rai, B.K.; Dwivedi, P. Spatial modeling of soil alkalinity in GIS environment using IRS data. In Proceedings of the 18th Asian Conference on Remote Sensing, Kuala Lumpur, Malaysia, 20–24 October 1997; pp. A.8.1–A.8.6.
48. Abbas, A.; Khan, S. Using remote sensing techniques for appraisal of irrigated soil salinity. In Proceedings of the International Congress on Modelling and Simulation (MODSIM), Christchurch, New Zealand, 10–13 December 2007; pp. 2632–2638.
49. Douaoui, A.E.K.; Nicolas, H.; Walter, C. Detecting salinity hazards within a semiarid context by means of combining soil and remote-sensing data. *Geoderma* **2006**, *134*, 217–230. [\[CrossRef\]](#)

50. Zhou, X.; Zhang, F.; Zhang, H.; Zhang, X.; Yuan, J. A study of soil salinity inversion based on multispectral remote sensing index in Ebinur lake wetland nature reserve. *Spectrosc. Spect. Anal.* **2019**, *39*, 1229–1235.
51. Zhu, X.; Helmer, E.H.; Gao, F.; Liu, D.; Chen, J.; Lefsky, M.A. A flexible spatiotemporal method for fusing satellite images with different resolutions. *Remote Sens. Environ.* **2016**, *172*, 165–177. [[CrossRef](#)]
52. Qi, S.; He, M.; Bai, Z.; Ding, Z.; Sandhu, P.; Chung, F.; Namadi, P.; Zhou, Y.; Hoang, R.; Tom, B. Novel Salinity Modeling Using Deep Learning for the Sacramento–San Joaquin Delta of California. *Water* **2022**, *14*, 3628. [[CrossRef](#)]
53. Feurer, M.; Hutter, F. Hyperparameter optimization. In *Automated Machine Learning*; Springer: New York, NY, USA, 2019; pp. 3–33.
54. Zhang, C.; Xue, Y. Estimation of Biochemical Pigment Content in Poplar Leaves Using Proximal Multispectral Imaging and Regression Modeling Combined with Feature Selection. *Sensors* **2023**, *24*, 217. [[CrossRef](#)]
55. Sun, G.; Zhu, Y.; Gao, Z.; Yang, J.; Qu, Z.; Mao, W.; Wu, J. Spatiotemporal patterns and key driving factors of soil salinity in dry and wet years in an arid agricultural area with shallow groundwater table. *Agriculture* **2022**, *12*, 1243. [[CrossRef](#)]
56. You, Q.; Deng, W.; Liu, Y.; Tang, X.; Chen, J.; You, H. Extraction the Spatial Distribution of Mangroves in the Same Month Based on Images Reconstructed with the FSDAF Model. *Forests* **2023**, *14*, 2399. [[CrossRef](#)]
57. Wang, Z.; Gao, Z.; Jiang, X. Analysis of the evolution and driving forces of tidal wetlands at the estuary of the Yellow River and Laizhou Bay based on remote sensing data cube. *Ocean Coast. Manag.* **2023**, *237*, 106535. [[CrossRef](#)]
58. Zhu, X.; Cai, F.; Tian, J.; Williams, T.K.-A. Spatiotemporal fusion of multisource remote sensing data: Literature survey, taxonomy, principles, applications, and future directions. *Remote Sens.* **2018**, *10*, 527. [[CrossRef](#)]
59. Belgiu, M.; Stein, A. Spatiotemporal image fusion in remote sensing. *Remote Sens.* **2019**, *11*, 818. [[CrossRef](#)]
60. Fu, C.; Tian, A.; Zhu, D.; Zhao, J.; Xiong, H. Estimation of salinity content in different saline-alkali zones based on machine learning model using FOD pretreatment method. *Remote Sens.* **2021**, *13*, 5140. [[CrossRef](#)]
61. Tan, J.; Ding, J.; Han, L.; Ge, X.; Wang, X.; Wang, J.; Wang, R.; Qin, S.; Zhang, Z.; Li, Y. Exploring PlanetScope Satellite Capabilities for Soil Salinity Estimation and Mapping in Arid Regions Oases. *Remote Sens.* **2023**, *15*, 1066. [[CrossRef](#)]
62. Shu, Q.; Xi, L.; Wang, K.; Xie, F.; Pang, Y.; Song, H. Optimization of samples for remote sensing estimation of forest aboveground biomass at the regional scale. *Remote Sens.* **2022**, *14*, 4187. [[CrossRef](#)]
63. Varma, S.; Simon, R. Bias in error estimation when using cross-validation for model selection. *BMC Bioinform.* **2006**, *7*, 91. [[CrossRef](#)]
64. Hao, S.; Abuduwaili, J. Spatial distribution of soil moisture and salinity and their influence factors in the farmland of Manas River catchment, Northwest China. *Chin. J. Appl. Ecol.* **2015**, *26*, 769–776.

Disclaimer/Publisher’s Note: The statements, opinions and data contained in all publications are solely those of the individual author(s) and contributor(s) and not of MDPI and/or the editor(s). MDPI and/or the editor(s) disclaim responsibility for any injury to people or property resulting from any ideas, methods, instructions or products referred to in the content.